Magnonic Quadrupole Topological Insulator in Antiskyrmion Crystals

Tomoki Hirosawa,[1] Sebastián A. Díaz,[2] Jelena Klinovaja,[2] and Daniel Loss[2]
[1]*Department of Physics, University of Tokyo, Bunkyo, Tokyo 113-0033, Japan*
[2]*Department of Physics, University of Basel, Klingelbergstrasse 82, CH-4056 Basel, Switzerland*

(Received 17 May 2020; revised 20 September 2020; accepted 15 October 2020; published 12 November 2020)

We uncover that antiskyrmion crystals provide an experimentally accessible platform to realize a magnonic quadrupole topological insulator, whose hallmark signatures are robust magnonic corner states. Furthermore, we show that tuning an applied magnetic field can trigger the self-assembly of antiskyrmions carrying a fractional topological charge along the sample edges. Crucially, these fractional antiskyrmions restore the symmetries needed to enforce the emergence of the magnonic corner states. Using the machinery of nested Wilson loops, adapted to magnonic systems supported by noncollinear magnetic textures, we demonstrate the quantization of the bulk quadrupole moment, edge dipole moments, and corner charges.

DOI: 10.1103/PhysRevLett.125.207204

Higher-order topological phases of matter in d-dimensional systems are characterized by the presence of in-gap states that belong to boundaries of dimension lower than $(d-1)$, namely, to hinges or corners [1–3]. Such states could be protected by crystalline symmetries, sometimes in conjunction with time reversal, or, alternatively, by particle-hole symmetry if superconductivity is involved [4–8]. Although they were initially postulated in electronic systems, they have been extended to include also bosonic excitations such as phonons [9–12] and photons [13–16]. A stringent requirement for the realization of these topological states is the local preservation of the protecting symmetries at the corresponding higher-order boundaries. Therefore, experimental realizations of higher-order topology usually involve careful engineering of the sample boundaries.

Magnons, the quanta of spin waves, are another bosonic excitation in condensed matter. While theoretical predictions of first-order topological magnonic states are abundant [17–29], so far there have been only a few reports on their higher-order counterparts [30]. This may be related to the fact that, in the vicinity of sample boundaries, the magnetization field can get easily deformed, making it difficult to preserve crystalline symmetries.

Among the two-dimensional magnetic platforms predicted to host first-order topological magnonic edge states are ferromagnetic and antiferromagnetic skyrmion crystals [26–29]. Magnetic skyrmions are microscopic, stable, swirling spin configurations characterized by an integer topological charge [31–34], which in the continuum is given by $Q = (1/4\pi)\int d^2 r\, \boldsymbol{m}\cdot(\partial_x \boldsymbol{m}\times\partial_y \boldsymbol{m})$, where $\boldsymbol{m} = \boldsymbol{M}/|\boldsymbol{M}|$ is the normalized magnetization field. The strict requirements for the integer-valuedness of the net topological charge are no longer met in confined systems, thus allowing a net fractional topological charge. In fact, skyrmion nucleation has been predicted to take place from the sample edges [35,36] through continuous growth of intermediate states with fractional topological charge. Isolated antiskyrmions, a kind of skyrmion with opposite topological charge, as well as antiskyrmion crystals were recently observed in acentric tetragonal Heusler compounds with D_{2d} crystal symmetry [37].

Here, we show that a magnonic quadrupole topological insulator can be realized in two-dimensional antiskyrmion crystals (Fig. 1). This second-order topological phase is protected by the combined effect of $C_{2x}\mathcal{T}$ and $C_{2y}\mathcal{T}$ symmetries, which quantize and render nontrivial the bulk quadrupole moment [1,2]. The expected robust magnonic corner states emerge only upon tuning the external magnetic field below a critical value, triggering the self-assembly of *fractional antiskyrmions* stabilized along the

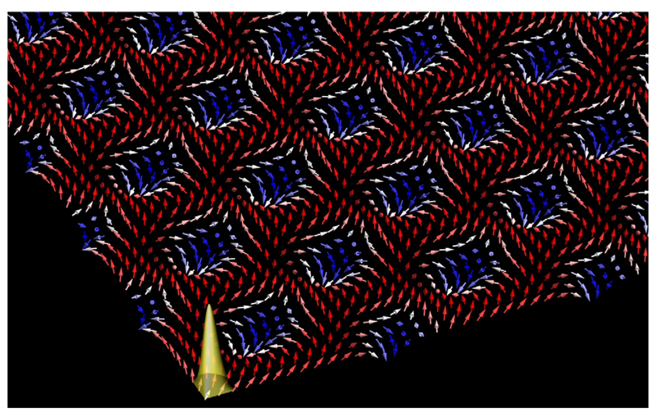

FIG. 1. Antiskyrmion crystals support topological magnonic corner states. Magnetic texture of an antiskyrmion crystal in the vicinity of a sample corner. Fractional antiskyrmions that self-assemble along the sample edge allow the emergence of a topological magnonic state whose probability amplitude (depicted in yellow) is corner localized.

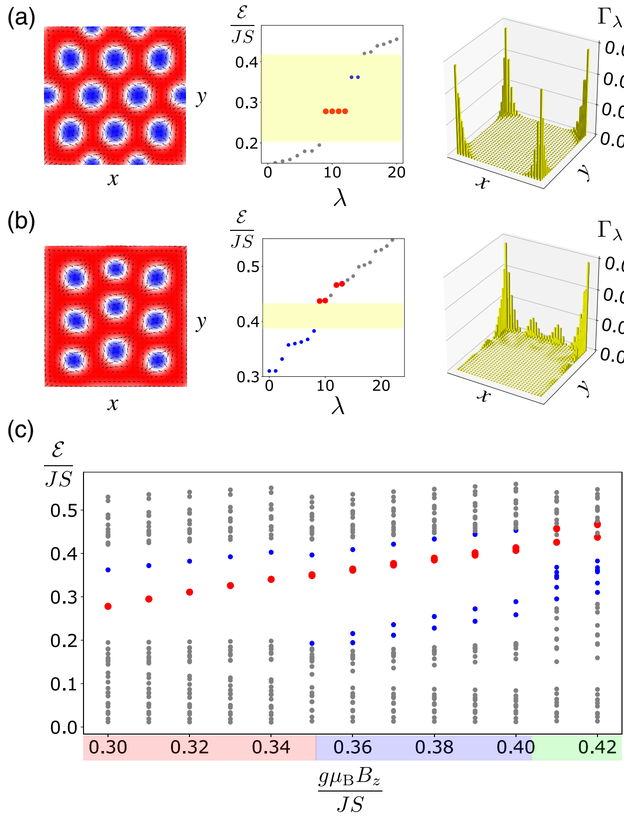

FIG. 2. Formation of magnonic corner states in confined antiskyrmion crystals. (a),(b) Characterization of confined antiskyrmion crystals at $g\mu_B B_z/(JS) = 0.3$ and $g\mu_B B_z/(JS) = 0.42$, respectively. Left: Classical ground-state magnetic texture. Middle: Magnon spectrum showing corner states (red) and trivial bound states (blue) localized at the fractional antiskyrmions away from the corners. Right: Probability density of the corner states, Γ_λ (defined in Ref. [38]). (c) Magnon spectrum against the applied magnetic field with corner and edge-localized states highlighted as in the above panels. The bottom color bar indicates different configurations with the configuration in (a) and (b) corresponding to the red and green region, respectively.

sample edges that restore the protecting symmetries (Fig. 2). Our modeling is inspired by the already available antiskyrmion-hosting Heusler compounds [37], in which our predictions could be experimentally tested. However, we emphasize that our results also apply to ferromagnetic skyrmion crystals (Supplemental Material [38]).

Antiskyrmion crystal model.—As a minimal model that can describe the magnetism of acentric tetragonal Heusler compounds, we consider the following two-dimensional spin lattice Hamiltonian:

$$H = \frac{1}{2}\sum_{\langle \boldsymbol{r},\boldsymbol{r}'\rangle}(-J_{\boldsymbol{r},\boldsymbol{r}'}\boldsymbol{S}_{\boldsymbol{r}}\cdot\boldsymbol{S}_{\boldsymbol{r}'} + \boldsymbol{D}_{\boldsymbol{r},\boldsymbol{r}'}\cdot\boldsymbol{S}_{\boldsymbol{r}}\times\boldsymbol{S}_{\boldsymbol{r}'}) - g\mu_B B_z\sum_{\boldsymbol{r}}\boldsymbol{S}_{\boldsymbol{r}}\cdot\hat{z}, \tag{1}$$

where $\boldsymbol{S}_{\boldsymbol{r}}$ is a spin operator at site $\boldsymbol{r}$ on a square lattice with lattice constant a. The nearest-neighbor coupling includes ferromagnetic exchange $J_{\boldsymbol{r},\boldsymbol{r}'} = J(\delta_{\boldsymbol{r}-\boldsymbol{r}',\pm a\hat{\boldsymbol{x}}} + \delta_{\boldsymbol{r}-\boldsymbol{r}',\pm a\hat{\boldsymbol{y}}})$ with $J > 0$ and Dzyaloshinskii-Moriya (DM) interaction $\boldsymbol{D}_{\boldsymbol{r},\boldsymbol{r}'} = D(\mp\hat{\boldsymbol{x}}\delta_{\boldsymbol{r}-\boldsymbol{r}',\pm a\hat{\boldsymbol{x}}} \pm \hat{\boldsymbol{y}}\delta_{\boldsymbol{r}-\boldsymbol{r}',\pm a\hat{\boldsymbol{y}}})$ consistent with D_{2d} crystal symmetry. Throughout this Letter, we take $D/J = 1.0$ for numerical simplicity [38]. The last term represents the coupling to the external magnetic field, $B_z\hat{\boldsymbol{z}}$, where g and μ_B denote the g factor and Bohr magneton, respectively. Dipolar interactions do not affect our results in the zero-thickness limit [38]; hence, we neglect them for simplicity.

The classical ground-state texture at zero temperature is obtained using Monte Carlo simulated annealing [47] and then minimizing the energy further by solving the atomistic Landau-Lifshitz-Gilbert equation [38]. A triangular crystal of antiskyrmions is found in the external magnetic field range $0.27 \leq g\mu_B B_z/(JS) \leq 0.7$.

It is convenient to introduce the rectangular enlarged magnetic unit cell (MUC) shown in Fig. 3(a), which encompasses two antiskyrmions and is commensurate with the underlying square lattice of spins. This MUC is

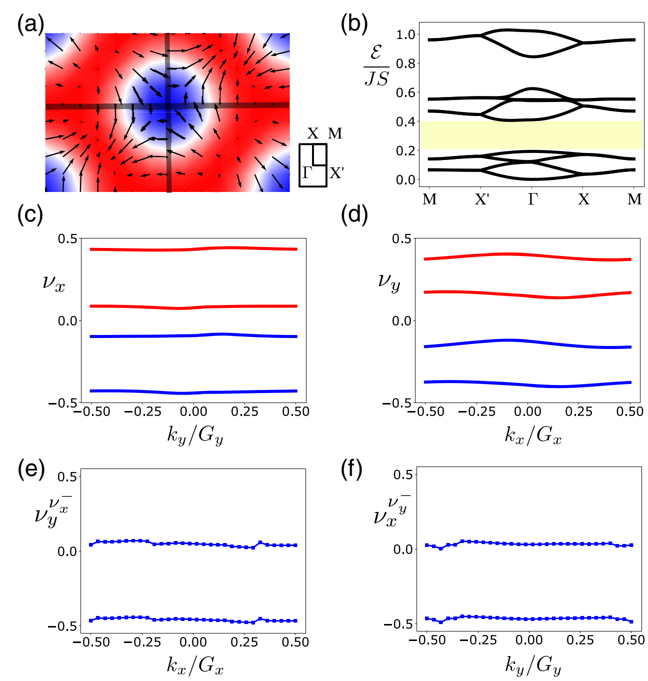

FIG. 3. Bulk symmetries and Wannier spectra in antiskyrmion crystals. (a) Magnetic unit cell of the antiskyrmion crystal with symmetry lines for $C_{2x/2y}$. The C_{2z} rotation axis is at the center of the magnetic unit cell. The first Brillouin zone is also shown. (b) Bulk magnon spectrum of the antiskyrmion crystal. The fourth bulk magnon gap is highlighted in yellow. (c),(d) Wannier spectrum of the four lowest-energy magnon bands showing the Wannier sector $\nu^+_{x/y}$ in red and $\nu^-_{x/y}$ in blue. (e),(f) Wannier centers of the Wannier sector $\nu^-_{x/y}$. For all panels, the magnetic field is $g\mu_B B_z/(JS) = 0.35$ and $G_{x/y} = 2\pi/(L_{x/y}a)$ with $L_{x/y}$ denoting the number of lattice sites in the magnetic unit cell along the x/y axis.

invariant under the action of either of the symmetry operations: C_{2z}, twofold rotation about the z axis; $C_{2x}\mathcal{T}$, twofold rotation about the x axis together with time reversal; and $C_{2y}\mathcal{T}$, twofold rotation about the y axis also together with time reversal. These are defined with respect to Cartesian axes with origin at the center of the MUC as depicted in Fig. 3(a).

Another consequence of adopting such an enlarged MUC that carries over to the spectrum of magnonic excitations is the doubling, due to backfolding, of the bulk magnon bands. For instance, Fig. 3(b) shows the bottom of the bulk magnon spectrum computed using the enlarged MUC. Details of the calculation of the magnon spectrum of the antiskyrmion crystal are in Ref. [38]. Lastly, the double degeneracy observed for all bands along the paths XM and MX' is the result of and is protected by $C_{2x}\mathcal{T}$ and $C_{2y}\mathcal{T}$ symmetries [38].

Fractional antiskyrmions and magnonic corner states.— When confined to finite-sized samples, the magnetic texture of antiskyrmion crystals exhibits a reconstruction with drastic consequences for the supported magnonic excitations. In the vicinity of the sample edges, a tendency to twist the magnetization is induced by the DM interaction which competes with the out-of-plane alignment favored by the magnetic field. For high field values, a twisted magnetic texture is attained along the edges [48,49], as seen in Fig. 2(b). As the field is lowered, a critical value B_c, with $g\mu_B B_c/(JS) \approx 0.41$, is reached, below which the edge texture becomes unstable to the nucleation of fractional antiskyrmions [38]. Because of their mutual repulsion, antiskyrmions from within the bulk stabilize the newly nucleated fractional antiskyrmions along the edges of the sample. This is confirmed by our field-cooling numerical simulations, which ensure the presence of an antiskyrmion crystal in the bulk. A similar edge instability behavior has been reported for skyrmions [36,50], but so far no edge-stabilized fractional skyrmions have been observed.

The magnon spectrum of a confined antiskyrmion crystal at $g\mu_B B_z/(JS) = 0.3$ with fractional antiskyrmions stabilized along the sample edge is shown in Fig. 2(a). Highlighted in red are four degenerate states which are well separated from the bulk states (gray). They correspond to corner states, one for each corner of the sample, which will be shown to originate from higher-order topology. There also exist topologically trivial bound states (blue) localized at the fractional antiskyrmions far away from the corners. On the other hand, at $g\mu_B B_z/(JS) = 0.42$, there are no fractional antiskyrmions [Fig. 2(b)]. Although four modes with significant probability density near the corners can still be identified, they are buried among bulk modes, and they spread over the edges and into the bulk of the sample.

A clearer picture emerges from plotting the magnon spectrum as a function of the applied magnetic field [Fig. 2(c)]. We first note that the bulk magnon gap where corner states are found corresponds to the fourth bulk magnon gap of the antiskyrmion crystal [Fig. 3(b)]. Remarkably, corner states emerge only when fractional antiskyrmions are stabilized along the sample edges, i.e., for $g\mu_B B_z/(JS) \leq 0.40$. In this range, the energies of corner states (red) and states localized at fractional antiskyrmions (blue) increase linearly with the applied field. These magnonic corner states are remarkably robust against the effect of magnetic impurity disorder [38]. Although their degeneracy is lifted by disorder, they remain isolated, avoiding hybridization with bulk modes. Furthermore, taking advantage of finite-size effects and introducing holes within the bulk of the sample, we show in Ref. [38] that magnonic corner states can be engineered at select corners and inside the sample, respectively.

Bulk quadrupole moment.—The robust magnonic corner states we have uncovered are, in fact, second-order topological magnonic states. More precisely, antiskyrmion crystals provide a platform to realize magnonic quadrupole topological insulators. This higher-order topological phase is protected by the combined action of $C_{2x}\mathcal{T}$ and $C_{2y}\mathcal{T}$ symmetries, resulting in a quantized bulk quadrupole moment. We use the nested Wilson loop construction, which we adapted to magnons to compute the bulk quadrupole moment [38].

Parallel transport in the subspace of occupied states over noncontractible loops in the Brillouin zone is equivalent to a unitary transformation whose matrix representation is called a Wilson loop. Crucially, the eigenvalues of the position operator along x/y projected on the subspace of occupied bands coincide with the complex phases of the Wilson loop eigenvalues along k_x/k_y, given by $2\pi\nu_x^j(k_y)/2\pi\nu_y^j(k_x)$ [51]. From this connection and because the eigenstates of the projected position operator are Wannier states, the $\nu_x^j(k_y)$ and $\nu_y^j(k_x)$ are called Wannier centers or Wannier spectra. They describe how magnons from the subspace of occupied bands distribute over the MUC.

Before computing the bulk quadrupole moment, the following three essential requirements must be fulfilled [2]: (i) The corner states lie within the nth bulk magnon gap with $n \geq 2$; (ii) the lowest n magnon bands carry a vanishing net Chern number; and (iii) the bulk dipole moment vanishes. As mentioned above, the magnonic corner states are found within the fourth bulk magnon gap. Also, the four bulk magnon bands below this gap carry no Chern number in the magnetic field range of interest. The bulk polarization of the occupied bands is defined as the dipole moment of the corresponding Wannier states, which is equivalent to a sum over Wannier centers [52]. Thus, the Cartesian components of the total bulk polarization are given by

$$p_x = \frac{1}{2\pi}\int dk_y \sum_{j=1}^{M} \nu_x^j(k_y) \mod 1, \tag{2}$$

$$p_y = \frac{1}{2\pi}\int dk_x \sum_{j=1}^{M} \nu_y^j(k_x) \mod 1, \tag{3}$$

where $M = 4$ is the number of bulk bands below the gap where the magnonic corner states are found. We show in Ref. [38] that the symmetries of the MUC translate into the following constraints on the Wannier spectra:

$$\nu_x^j(k_y) \overset{C_{2y}\mathcal{T}}{=} -\nu_x^j(-k_y) \mod 1, \tag{4}$$

$$\nu_y^j(k_x) \overset{C_{2x}\mathcal{T}}{=} -\nu_y^j(-k_x) \mod 1. \tag{5}$$

Therefore, ν_x^j can be constant and equal to either 0 or $\frac{1}{2}$, the other possibility being that it has a partner $\nu_x^{j'}$ such that $\nu_x^j(k_y) = -\nu_x^{j'}(-k_y)$. Similar allowed values can be expected for ν_y^j. Figures 3(c) and 3(d) show the Wannier spectra of the lowest four bulk magnon bands. The absence of flat Wannier bands at $\frac{1}{2}$ implies that the bulk dipole moment vanishes, i.e., $(p_x, p_y) = (0, 0)$.

Now that we have established the fulfillment of the above three desiderata, we proceed to compute the bulk quadrupole moment. As shown in Figs. 3(c) and 3(d), the Wannier spectra can be separated into two Wannier sectors corresponding to the subspaces of magnonic states that localize along the positive (red) and negative (blue) x/y directions of the MUC (the origin of coordinates is located at its center). Within each of these subspaces, the nested Wilson loops can be constructed (details in Ref. [38]). Figure 3(e) depicts the Wannier centers $\nu_y^{\nu_x^-,p}(k_x)$ of the nested Wilson loop along k_y of the Wannier sector ν_x^-, which indicate the localization along the y direction of the subspace of magnonic states that are localized toward the negative x direction. Similarly, Fig. 3(f) shows the Wannier centers $\nu_x^{\nu_y^-,p}(k_y)$ of the nested Wilson loop along k_x of the Wannier sector ν_y^-. These Wannier centers from positive and negative Wannier sectors determine the Wannier sector polarizations

$$p_y^{\nu_x^\pm} = \frac{1}{2\pi}\int dk_x \sum_{p=1}^{2} \nu_y^{\nu_x^\pm,p}(k_x) \mod 1, \tag{6}$$

$$p_x^{\nu_y^\pm} = \frac{1}{2\pi}\int dk_y \sum_{p=1}^{2} \nu_x^{\nu_y^\pm,p}(k_y) \mod 1, \tag{7}$$

which, in turn, are used to define the bulk quadrupole moment

$$q_{xy} = p_y^{\nu_x^+} p_x^{\nu_y^+} + p_y^{\nu_x^-} p_x^{\nu_y^-}. \tag{8}$$

Although not critical to our results, constraints from C_{2z} symmetry on the nested Wilson loop eigenvalues further simplify it to $q_{xy} = 2p_y^{\nu_x^-} p_x^{\nu_y^-}$. The Wannier bands needed to compute $p_y^{\nu_x^-}$ and $p_x^{\nu_y^-}$ are shown in Figs. 3(e) and 3(f). As constrained by $C_{2x}\mathcal{T}$ and $C_{2y}\mathcal{T}$ symmetries, within numerical error, one of the bands is quantized to 0 and the other to $-\frac{1}{2}$. Therefore, we obtain $p_x^{\nu_y^-} = p_y^{\nu_x^-} = -\frac{1}{2}$, which implies the quantization of the bulk quadrupole moment to $q_{xy} = \frac{1}{2}$.

Furthermore, our numerical calculations show that the bulk quadrupole moment is quantized for any value of the external magnetic field, as long as the antiskyrmion crystal remains stable.

Bulk-boundary correspondence and fractional antiskyrmions.—The emergence of magnonic corner states is not guaranteed by a quantized bulk quadrupole moment. Boundaries must also preserve the protecting $C_{2x}\mathcal{T}$ and $C_{2y}\mathcal{T}$ symmetries. At high applied fields, even though the bulk quadrupole moment is quantized, no magnonic corner states are realized, because the magnetic texture of the antiskyrmion crystal is distorted near the sample boundaries [Fig. 2(b)], thus breaking the protecting symmetries. Decreasing the magnetic field below the critical value B_c triggers the nucleation of fractional antiskyrmions from the sample boundaries. The newly formed fractional antiskyrmions play the role of the nearest neighbors missing from antiskyrmions located near the edge of the sample. Therefore, by virtue of their mutual repulsion with bulk antiskyrmions, fractional antiskyrmions self-assemble along the sample edges. This process restores the protecting symmetries, thus allowing the formation of magnonic corner states.

Two hallmark signatures are expected of a quantized quadrupole moment: edge dipole moments and corner charges. These should also be quantized in a manner consistent with the bulk quadrupole, i.e., $q_{xy} = |p_x^{\text{edge}}| = |p_y^{\text{edge}}| = |Q_c|$. The edges of the sample are themselves topological insulating, and the corner states are simultaneous end states of two converging edges [1,2]. Therefore, as an initial consistency check, we can just count the number of magnonic corner states. Only one such state is expected at each corner.

To compute the edge dipole moments, we study the antiskyrmion crystal in a strip geometry [38]. Indeed, we find that, only for applied fields below B_c, the edge dipole moments are quantized to $|p_x^{\text{edge}}| = |p_y^{\text{edge}}| = \frac{1}{2}$ with opposite signs at opposite edges.

Although magnons carry no electric charge, we can still introduce a quantity similar to the electric boundary charges [53–59] constructed out of magnon number densities. The fractional corner "charge" carried by the lowest four bulk magnon bands of the antiskyrmion crystal in a finite system is given by [60]

$$Q_c = \sum_{\boldsymbol{r}\in\text{one sector}} \phi(\boldsymbol{r}) \mod 1, \tag{9}$$

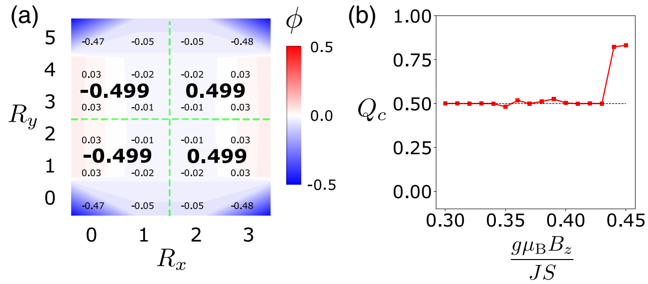

FIG. 4. Fractional corner charges induced by the quantized bulk quadrupole moment. (a) The value of the magnon charge density $\phi(\boldsymbol{r})$ of a 60×60 spin lattice at $g\mu_B B_z/(JS) = 0.3$ is indicated for each magnetic unit cell, which are labeled by R_x and R_y. Green dashed lines divide the sample into four symmetry sectors whose net magnon charge is denoted by large bold numbers. The corner charge Q_c obtained from each symmetry sector is equal to $\frac{1}{2}$. (b) The magnetic field dependence of Q_c, obtained by relaxing the classical ground-state configuration at $g\mu_B B_z/JS = 0.3$ as the field is gradually increased. Q_c remains quantized at $\frac{1}{2}$ below the edge instability critical field and exhibits a sudden increase above it, signaling a topological phase transition.

with $\phi(\boldsymbol{r}) = \rho(\boldsymbol{r}) - [\rho_1(\boldsymbol{r}) + \rho_2(\boldsymbol{r})]$, where $\rho(\boldsymbol{r})$ is the magnon density of the finite system and $\rho_1(\boldsymbol{r})/\rho_2(\boldsymbol{r})$ is the magnon density of a 1D periodic system along the x/y axis (precise definitions in Ref. [38]). $C_{2x}\mathcal{T}$ and $C_{2y}\mathcal{T}$ define four equivalent symmetry sectors [separated by green dashed lines in Fig. 4(a)], and the magnon charge density $\phi(\boldsymbol{r})$ is summed over one of them to obtain Q_c. Figure 4(a) clearly shows the magnon charge density is corner localized and Q_c is quantized to $\frac{1}{2}$ at each symmetry sector. As a function of the magnetic field, depicted in Fig. 4(b), Q_c remains quantized below and suddenly increases above the edge instability critical field, signaling a topological phase transition.

Conclusions.—We have uncovered that antiskyrmion crystals can realize a magnonic quadrupole topological insulator. Tuning an applied magnetic field induces the self-assembly of fractional antiskyrmions along the edges of the sample. Remarkably, these fractional antiskyrmions restore the protecting symmetries that allow the formation of robust magnonic corner states. Acentric tetragonal Heusler compounds, where antiskyrmion crystals and edge fractional objects have already been observed, constitute an ideal platform to test our findings. But we note that our theory also applies to ferromagnetic skyrmion crystals, where the protecting symmetries for Bloch and Néel skyrmions, also symmetries of the MUC, are $\{C_{2x}\mathcal{T}, C_{2y}\mathcal{T}\}$ and $\{M_x\mathcal{T}, M_y\mathcal{T}\}$, respectively [38]. The magnonic corner states energy can be measured by ferromagnetic resonance spectroscopy. An ac magnetic field can selectively excite the corner states, and then their spatial distribution can be measured with NV center magnetometry [61] or near-field Brillouin light scattering [62]. Since Q_c is defined in terms of magnon densities, the aforementioned techniques can be used to measure it as in Ref. [60]. Magnonic corner states can be used as a magnon cavity [63] with a high Q factor [14] to enhance magnon-photon [64,65] interactions for quantum computing and quantum information applications. Our study highlights a new form of topological excitation in magnetic systems and its potential use in the design of future magnonic devices.

We are grateful to A. Mook, I. Tateishi, T. Hinokihara, H. Matsuura, M. Ogata, M. Nagao, T. Nagase, and D. Shimizu for useful discussions. T. H. is supported by Japan Society for the Promotion of Science (JSPS) through Program for Leading Graduate Schools (MERIT) and JSPS KAKENHI (Grant No. 18J21985). This work was supported by the Swiss National Science Foundation and NCCR QSIT. This project received funding from the European Union's Horizon 2020 research and innovation program (ERC Starting Grant, Grant Agreement No. 757725).

[1] W. A. Benalcazar, B. A. Bernevig, and T. L. Hughes, Quantized electric multipole insulators, Science **357**, 61 (2017).
[2] W. A. Benalcazar, B. A. Bernevig, and T. L. Hughes, Electric multipole moments, topological multipole moment pumping, and chiral hinge states in crystalline insulators, Phys. Rev. B **96**, 245115 (2017).
[3] F. Schindler, A. M. Cook, M. G. Vergniory, Z. Wang, S. S. P. Parkin, B. A. Bernevig, and T. Neupert, Higher-order topological insulators, Sci. Adv. **4** (2018).
[4] Y. Volpez, D. Loss, and J. Klinovaja, Second-Order Topological Superconductivity in π-Junction Rashba Layers, Phys. Rev. Lett. **122**, 126402 (2019).
[5] S. Franca, D. V. Efremov, and I. C. Fulga, Phase-tunable second-order topological superconductor, Phys. Rev. B **100**, 075415 (2019).
[6] J. Langbehn, Y. Peng, L. Trifunovic, F. von Oppen, and P. W. Brouwer, Reflection-Symmetric Second-Order Topological Insulators and Superconductors, Phys. Rev. Lett. **119**, 246401 (2017).
[7] Y. Wang, M. Lin, and T. L. Hughes, Weak-pairing higher order topological superconductors, Phys. Rev. B **98**, 165144 (2018).
[8] K. Plekhanov, F. Ronetti, D. Loss, and J. Klinovaja, Hinge states in a system of coupled Rashba layers, Phys. Rev. Res. **2**, 013083 (2020).
[9] M. Serra-Garcia, V. Peri, R. Süsstrunk, O. R. Bilal, T. Larsen, L. G. Villanueva, and S. D. Huber, Observation of a phononic quadrupole topological insulator, Nature (London) **555**, 342 (2018).
[10] X. Ni, M. Weiner, A. Alù, and A. B. Khanikaev, Observation of higher-order topological acoustic states protected by generalized chiral symmetry, Nat. Mater. **18**, 113 (2019).
[11] H. Fan, B. Xia, L. Tong, S. Zheng, and D. Yu, Elastic Higher-Order Topological Insulator with Topologically Protected Corner States, Phys. Rev. Lett. **122**, 204301 (2019).
[12] H. Xue, Y. Yang, F. Gao, Y. Chong, and B. Zhang, Acoustic higher-order topological insulator on a kagome lattice, Nat. Mater. **18**, 108 (2019).

[13] B.-Y. Xie, H.-F. Wang, H.-X. Wang, X.-Y. Zhu, J.-H. Jiang, M.-H. Lu, and Y.-F. Chen, Second-order photonic topological insulator with corner states, Phys. Rev. B **98**, 205147 (2018).
[14] X.-D. Chen, W.-M. Deng, F.-L. Shi, F.-L. Zhao, M. Chen, and J.-W. Dong, Direct Observation of Corner States in Second-Order Topological Photonic Crystal Slabs, Phys. Rev. Lett. **122**, 233902 (2019).
[15] B.-Y. Xie, G.-X. Su, H.-F. Wang, H. Su, X.-P. Shen, P. Zhan, M.-H. Lu, Z.-L. Wang, and Y.-F. Chen, Visualization of Higher-Order Topological Insulating Phases in Two-Dimensional Dielectric Photonic Crystals, Phys. Rev. Lett. **122**, 233903 (2019).
[16] S. Mittal, V. V. Orre, G. Zhu, M. A. Gorlach, A. Poddubny, and M. Hafezi, Photonic quadrupole topological phases, Nat. Photonics **13**, 692 (2019).
[17] R. Shindou, R. Matsumoto, S. Murakami, and J.-i. Ohe, Topological chiral magnonic edge mode in a magnonic crystal, Phys. Rev. B **87**, 174427 (2013).
[18] L. Zhang, J. Ren, J.-S. Wang, and B. Li, Topological magnon insulator in insulating ferromagnet, Phys. Rev. B **87**, 144101 (2013).
[19] A. Mook, J. Henk, and I. Mertig, Edge states in topological magnon insulators, Phys. Rev. B **90**, 024412 (2014).
[20] R. Chisnell, J. S. Helton, D. E. Freedman, D. K. Singh, R. I. Bewley, D. G. Nocera, and Y. S. Lee, Topological Magnon Bands in a Kagome Lattice Ferromagnet, Phys. Rev. Lett. **115**, 147201 (2015).
[21] A. Mook, J. Henk, and I. Mertig, Spin dynamics simulations of topological magnon insulators: From transverse current correlation functions to the family of magnon Hall effects, Phys. Rev. B **94**, 174444 (2016).
[22] S. A. Owerre, A first theoretical realization of honeycomb topological magnon insulator, J. Phys. Condens. Matter **28**, 386001 (2016).
[23] K. Nakata, J. Klinovaja, and D. Loss, Magnonic quantum Hall effect and Wiedemann-Franz law, Phys. Rev. B **95**, 125429 (2017).
[24] K. Nakata, S. K. Kim, J. Klinovaja, and D. Loss, Magnonic topological insulators in antiferromagnets, Phys. Rev. B **96**, 224414 (2017).
[25] A. Rückriegel, A. Brataas, and R. A. Duine, Bulk and edge spin transport in topological magnon insulators, Phys. Rev. B **97**, 081106(R) (2018).
[26] A. Roldán-Molina, A. S. Nunez, and J. Fernández-Rossier, Topological spin waves in the atomic-scale magnetic skyrmion crystal, New J. Phys. **18**, 045015 (2016).
[27] S. K. Kim, K. Nakata, D. Loss, and Y. Tserkovnyak, Tunable Magnonic Thermal Hall Effect in Skyrmion Crystal Phases of Ferrimagnets, Phys. Rev. Lett. **122**, 057204 (2019).
[28] S. A. Díaz, J. Klinovaja, and D. Loss, Topological Magnons and Edge States in Antiferromagnetic Skyrmion Crystals, Phys. Rev. Lett. **122**, 187203 (2019).
[29] S. A. Díaz, T. Hirosawa, J. Klinovaja, and D. Loss, Chiral magnonic edge states in ferromagnetic skyrmion crystals controlled by magnetic fields, Phys. Rev. Res. **2**, 013231 (2020).
[30] A. Sil and A. K. Ghosh, First and second order topological phases on ferromagnetic breathing kagome lattice, J. Phys. Condens. Matter **32**, 205601 (2020).
[31] N. Nagaosa and Y. Tokura, Topological properties and dynamics of magnetic skyrmions, Nat. Nanotechnol. **8**, 899 (2013).
[32] A. Fert, N. Reyren, and V. Cros, Magnetic skyrmions: Advances in physics and potential applications, Nat. Rev. Mater. **2**, 17031 (2017).
[33] N. Kanazawa, S. Seki, and Y. Tokura, Noncentrosymmetric Magnets Hosting Magnetic Skyrmions, Adv. Mater. **29**, 1603227 (2017).
[34] K. Everschor-Sitte, J. Masell, R. M. Reeve, and M. Kläui, Perspective: Magnetic skyrmions—Overview of recent progress in an active research field, J. Appl. Phys. **124**, 240901 (2018).
[35] J. Iwasaki, M. Mochizuki, and N. Nagaosa, Current-induced skyrmion dynamics in constricted geometries, Nat. Nanotechnol. **8**, 742 (2013).
[36] H. Du, R. Che, L. Kong, X. Zhao, C. Jin, C. Wang, J. Yang, W. Ning, R. Li, C. Jin, X. Chen, J. Zang, Y. Zhang, and M. Tian, Edge-mediated skyrmion chain and its collective dynamics in a confined geometry, Nat. Commun. **6**, 8504 (2015).
[37] A. K. Nayak, V. Kumar, T. Ma, P. Werner, E. Pippel, R. Sahoo, F. Damay, U. K. Rößler, C. Felser, and S. S. P. Parkin, Magnetic antiskyrmions above room temperature in tetragonal Heusler materials, Nature (London) **548**, 561 (2017).
[38] See Supplemental Material at http://link.aps.org/supplemental/10.1103/PhysRevLett.125.207204 for spin wave Hamiltonian; atomistic spin dynamics; robustness against disorder; calculation of the bulk quadrupole moment, edge dipole moments and magnon corner charge; engineering of corner states; effect of dipolar and magnon-magnon interactions; and extension to ferromagnetic skyrmion crystals, which includes Refs. [39–46].
[39] T. Holstein and H. Primakoff, Field dependence of the intrinsic domain magnetization of a ferromagnet, Phys. Rev. **58**, 1098 (1940).
[40] J. H. P. Colpa, Diagonalization of the quadratic boson hamiltonian, Physica (Amsterdam) **93A**, 327 (1978).
[41] M. N. Wilson, E. A. Karhu, D. P. Lake, A. S. Quigley, S. Meynell, A. N. Bogdanov, H. Fritzsche, U. K. Rößler, and T. L. Monchesky, Discrete helicoidal states in chiral magnetic thin films, Phys. Rev. B **88**, 214420 (2013).
[42] H. Watanabe and M. Oshikawa, Inequivalent Berry Phases for the Bulk Polarization, Phys. Rev. X **8**, 021065 (2018).
[43] D. Song, Z.-A. Li, J. Caron, A. Kovács, H. Tian, C. Jin, H. Du, M. Tian, J. Li, J. Zhu, and R. E. Dunin-Borkowski, Quantification of Magnetic Surface and Edge States in an FeGe Nanostripe by Off-Axis Electron Holography, Phys. Rev. Lett. **120**, 167204 (2018).
[44] A. Mook, J. Klinovaja, and D. Loss, Quantum damping of skyrmion crystal eigenmodes due to spontaneous quasiparticle decay, Phys. Rev. Res. **2**, 033491 (2020).
[45] M. Garst, J. Waizner, and D. Grundler, Collective spin excitations of helices and magnetic skyrmions: Review and perspectives of magnonics in non-centrosymmetric magnets, J. Phys. D **50**, 293002 (2017).
[46] H. Y. Kwon, K. M. Bu, Y. Z. Wu, and C. Won, Effect of anisotropy and dipole interaction on long-range order

magnetic structures generated by Dzyaloshinskii-Moriya interaction, J. Magn. Magn. Mater. **324**, 2171 (2012).
[47] R. F. L. Evans, W. J. Fan, P. Chureemart, T. A. Ostler, M. O. A. Ellis, and R. W. Chantrell, Atomistic spin model simulations of magnetic nanomaterials, J. Phys. Condens. Matter **26**, 103202 (2014).
[48] S. Rohart and A. Thiaville, Skyrmion confinement in ultrathin film nanostructures in the presence of Dzyaloshinskii-Moriya interaction, Phys. Rev. B **88**, 184422 (2013).
[49] S. A. Meynell, M. N. Wilson, H. Fritzsche, A. N. Bogdanov, and T. L. Monchesky, Surface twist instabilities and skyrmion states in chiral ferromagnets, Phys. Rev. B **90**, 014406 (2014).
[50] J. Müller, A. Rosch, and M. Garst, Edge instabilities and skyrmion creation in magnetic layers, New J. Phys. **18**, 065006 (2016).
[51] A. Alexandradinata, X. Dai, and B. A. Bernevig, Wilson-loop characterization of inversion-symmetric topological insulators, Phys. Rev. B **89**, 155114 (2014).
[52] D. Vanderbilt, *Berry Phases in Electronic Structure Theory: Electric Polarization, Orbital Magnetization and Topological Insulators* (Cambridge University Press, Cambridge, England, 2018).
[53] W. P. Su, J. R. Schrieffer, and A. J. Heeger, Solitons in Polyacetylene, Phys. Rev. Lett. **42**, 1698 (1979).
[54] W. P. Su and J. R. Schrieffer, Fractionally Charged Excitations in Charge-Density-Wave Systems with Commensurability 3, Phys. Rev. Lett. **46**, 738 (1981).
[55] R. Jackiw and J. R. Schrieffer, Solitons with fermion number 12 in condensed matter and relativistic field theories, Nucl. Phys. **B190**, 253 (1981).
[56] J.-H. Park, G. Yang, J. Klinovaja, P. Stano, and D. Loss, Fractional boundary charges in quantum dot arrays with density modulation, Phys. Rev. B **94**, 075416 (2016).
[57] M. Thakurathi, J. Klinovaja, and D. Loss, From fractional boundary charges to quantized Hall conductance, Phys. Rev. B **98**, 245404 (2018).
[58] M. Pletyukhov, D. M. Kennes, J. Klinovaja, D. Loss, and H. Schoeller, Topological invariants to characterize universality of boundary charge in one-dimensional insulators beyond symmetry constraints, Phys. Rev. B **101**, 161106(R) (2020).
[59] M. Pletyukhov, D. M. Kennes, J. Klinovaja, D. Loss, and H. Schoeller, Surface charge theorem and topological constraints for edge states: Analytical study of one-dimensional nearest-neighbor tight-binding models, Phys. Rev. B **101**, 165304 (2020).
[60] C. W. Peterson, T. Li, W. A. Benalcazar, T. L. Hughes, and G. Bahl, A fractional corner anomaly reveals higher-order topology, Science **368**, 1114 (2020).
[61] C. M. Purser, V. P. Bhallamudi, F. Guo, M. R. Page, Q. Guo, G. D. Fuchs, and P. C. Hammel, Spinwave detection by nitrogen-vacancy centers in diamond as a function of probe–sample separation, Appl. Phys. Lett. **116**, 202401 (2020).
[62] J. Jersch, V. E. Demidov, H. Fuchs, K. Rott, P. Krzysteczko, J. Münchenberger, G. Reiss, and S. O. Demokritov, Mapping of localized spin-wave excitations by near-field brillouin light scattering, Appl. Phys. Lett. **97**, 152502 (2010).
[63] H. Huebl, C. W. Zollitsch, J. Lotze, F. Hocke, M. Greifenstein, A. Marx, R. Gross, and S. T. B. Goennenwein, High Cooperativity in Coupled Microwave Resonator Ferrimagnetic Insulator Hybrids, Phys. Rev. Lett. **111**, 127003 (2013).
[64] Y. Tabuchi, S. Ishino, A. Noguchi, T. Ishikawa, R. Yamazaki, K. Usami, and Y. Nakamura, Coherent coupling between a ferromagnetic magnon and a superconducting qubit, Science **349**, 405 (2015).
[65] Y. Li, T. Polakovic, Y.-L. Wang, J. Xu, S. Lendinez, Z. Zhang, J. Ding, T. Khaire, H. Saglam, R. Divan, J. Pearson, W.-K. Kwok, Z. Xiao, V. Novosad, A. Hoffmann, and W. Zhang, Strong Coupling Between Magnons and Microwave Photons in On-Chip Ferromagnet-Superconductor Thin-Film Devices, Phys. Rev. Lett. **123**, 107701 (2019).